The collisional depolarization of OH(A $^2\Sigma^+$) and NO(A $^2\Sigma^+$) with Kr

H. Chadwick,[1,a)] M. Brouard,[1,b)] Y.-P. Chang,[1,c)] C. J. Eyles,[1] G. McCrudden,[1] T. Perkins,[1] S. A. Seamons,[1] J. Kłos,[2,d)] M. H. Alexander,[3,e)] P. J. Dagdigian,[4,f)] D. Herráez-Aguilar,[5] and F. J. Aoiz[5,g)]

[1]*The Department of Chemistry, The Physical and Theoretical Chemistry Laboratory, University of Oxford, South Parks Road, Oxford OX1 3QZ, United Kingdom*
[2]*Department of Chemistry and Biochemistry, University of Maryland, College Park, Maryland 20742, USA*
[3]*Department of Chemistry and Biochemistry and Institute of Physical Science and Technology, University of Maryland, College Park, Maryland 20742, USA*
[4]*Department of Chemistry, The Johns Hopkins University, Baltimore, Maryland 21218, USA*
[5]*Departamento de Química Física, Facultad de Química, Universidad Complutense, 28040 Madrid, Spain*

(Received 19 November 2013; accepted 13 January 2014; published online 4 February 2014)

Quantum beat spectroscopy has been used to measure rate coefficients at 300 K for collisional depolarization for NO(A $^2\Sigma^+$) and OH(A $^2\Sigma^+$) with krypton. Elastic depolarization rate coefficients have also been determined for OH(A) + Kr, and shown to make a much more significant contribution to the total depolarization rate than for NO(A) + Kr. While the experimental data for NO(A) + Kr are in excellent agreement with single surface quasiclassical trajectory (QCT) calculations carried out on the upper $2A'$ potential energy surface, the equivalent QCT and quantum mechanical calculations cannot account for the experimental results for OH(A) + Kr collisions, particularly at low N. This disagreement is due to the presence of competing electronic quenching at low N, which requires a multi-surface, non-adiabatic treatment. Somewhat improved agreement with experiment is obtained by means of trajectory surface hopping calculations that include non-adiabatic coupling between the ground $1A'$ and excited $2A'$ states of OH(X/A) + Kr, although the theoretical depolarization cross sections still significantly overestimate those obtained experimentally. © *2014 AIP Publishing LLC*. [http://dx.doi.org/10.1063/1.4863446]

I. INTRODUCTION

Angular momentum polarization plays an important role in many physical and chemical processes.[1,2] Knowledge of angular momentum polarization is of practical importance in the quantitative interpretation of atomic and molecular spectra.[3] It is central to all photon-induced processes, including photoionization and photodissociation, due to the inherent anisotropic nature of the absorption and emission of light.[1,4–6] Rotational angular momentum polarization also plays a fundamental role in collisional studies involving reactants prepared in molecular beams or with polarized light.[2,7] The present study focusses on the collisional angular momentum depolarization of an initially polarized ensemble of molecules. Collisional angular momentum depolarization in elastic and inelastic scattering has come under the spotlight recently.[8–31] This work has generally focussed on the collisions of simple open shell molecules with a range of collision partners. Such studies are of interest as they provide fundamental insight into the dynamics of elastic and inelastic scattering.

Here we follow our previous studies on the collisional depolarization of OH(A) and NO(A) with He and Ar[8–17] by applying the quantum beat technique[32] to help elucidate the dynamics of both inelastic rotational energy transfer (RET)[33] and elastic collisions of OH(A) and NO(A) with krypton. In the NO(A) + Kr system, as in our previous studies of OH(A) and NO(A) with He and Ar,[8–11,13–16] electronic quenching of the excited radical is negligible and the experimental data are very well accounted for by theoretical calculations performed on the $2A'$ excited adiabatic potential energy surface (PES). This is in strong contrast with OH(A) + Kr collisions, where the electronic quenching cross section is on the order of 8 Å^2 under thermal conditions.[34,35] For OH(A) + Kr, electronic quenching proceeds *via* a conical intersection in the near-linear HO–Kr configuration.[35] This is close to the global, deep minimum of the OH(A) + Kr PES (0.76 eV),[17] which is in the same highly anisotropic region of the potential that is expected to be mostly responsible for RET and collisional depolarization in those collisions which remain on the electronically excited potential. It is therefore expected that rotational energy transfer and collisional depolarization of OH(A) by Kr will be in direct competition with electronic quenching, and the effect of quenching will be evident in the RET and collisional depolarization cross sections reported here.

The outline of the paper is as follows. Section II describes the experimental and theoretical procedures employed, and

a)Present address: Laboratoire de Chimie Physique Moléculaire, Ecole Polytechnique Fédérale de Lausanne, Switzerland
b)Electronic mail: mark.brouard@chem.ox.ac.uk
c)Present address: Center for Free-Electron Laser Science, Deutsches Elektronen-Synchrotron, Hamburg, Germany
d)Electronic mail: jklos@umd.edu
e)Electronic mail: mha@umd.edu
f)Electronic mail: pjdagdigian@jhu.edu
g)Electronic mail: aoiz@quim.ucm.es

the methods used to analyze the quantum beats. In Sec. III, we present the state-selected angular momentum depolarization cross sections for collisions of OH(A) and NO(A) with Kr recorded at 300 K. For OH(A) + Kr, elastic depolarization cross sections are also reported under thermal conditions. The experimental results are compared with results from quasiclassical trajectory (QCT) calculations performed using the latest *ab initio* potential energy surfaces (PESs) of Kłos *et al.* for NO(A) + Kr[36] and for OH(A) + Kr.[17] For the OH(A,X) + Kr system, trajectory surface-hopping QCT (TSH-QCT) calculations were also performed on the coupled PESs for OH(A) + Kr and OH(X) + Kr.[35] A discussion of these results follows in Sec. IV. The final section summarizes our principal conclusions.

II. METHOD

A. General theory

As in our previous work,[9–11,13,14,16] in the following $\boldsymbol{N}$ ($\boldsymbol{N}'$) denotes the diatomic rotational angular momentum apart from electron and nuclear spin. For a diatomic radical in a $^2\Sigma^+$ electronic state, for which electronic orbital angular momentum is zero, $\boldsymbol{N}$ ($\boldsymbol{N}'$) is equivalent to the nuclear rotational angular momentum, which must lie perpendicular to the internuclear axis, $\boldsymbol{r}$. The corresponding quantum number is written N (N'). The total rotational angular momentum apart from nuclear spin of OH(A) and NO(A) is denoted by $\boldsymbol{j}$, and its quantum number as j. In the Hund's case (b) coupling scheme appropriate for $^2\Sigma^+$ radicals, the molecular wave function is defined by $\boldsymbol{j} = \boldsymbol{N} + \boldsymbol{S}$, where $\boldsymbol{S}$ is the electronic spin. Since for both molecules $S = 1/2$, spin-rotation states for which $j = N + 1/2$ are termed as f_1 states, and those for which $j = N - 1/2$ are f_2. The total angular momentum quantum number of the collision system (i.e., NO(A) and OH(A) with Kr in the application discussed in Secs. II and III) is denoted by J.

The quantities measured in the present experiments are collisional depolarization rate coefficients, which can be converted into velocity averaged cross sections (see below). These depolarization cross sections can be thought of as measures of the $\boldsymbol{j}$-$\boldsymbol{j}'$ vector correlation,[10,15,16,37–39] which quantifies the tilt of the angular momentum subsequent to a collision. In both the classical and quantal descriptions of collisional depolarization, it is possible to relate the polarization moments *after* a collision, $\mathcal{P}_q^{(k)}(j')$, to the *extrinsic* moments of the initial state, $r_q^{(k)}(j)$, related to the preparation of j in the laboratory (LAB) frame, by[10,37,38]

$$\mathcal{P}_q^{(k)}(j') = a^{(k)}(j, j')\, r_q^{(k)}(j). \tag{1}$$

This equation is valid provided neither the initial nor the final directions of motion are defined, i.e., averaging over the initial and final relative velocities. Classically, it is readily shown that the depolarization moments (or multipole transfer coefficients[30,31]), $a^{(k)}(j, j')$, are directly related to the $\boldsymbol{j}$-$\boldsymbol{j}'$ vector correlation by the probability density function[10,15]

$$P(\theta_{jj'}) = \frac{1}{2}\sum_k [k] a^{(k)}(j, j') P_k(\cos\theta_{jj'}), \tag{2}$$

where $[k] = (2k + 1)$, $P_k(\cos\theta_{jj'})$ is the kth Legendre polynomial, and the depolarization moments are defined as

$$a^{(k)}(j, j') = \langle P_k(\cos\theta_{jj'})\rangle. \tag{3}$$

Note that only the $k = 1$ orientation moment and $k = 2$ alignment moment are considered in the present work, since these are the only non-zero values of $r_q^{(k)}(j)$ that can be generated with single photon excitation to produce the initial distribution of OH(A) and NO(A).

The quantum mechanical calculation of the depolarization moments has been discussed in detail in a number of papers.[10,26–28,37,38] When the initial and final directions of motion are unresolved, the multipole transfer coefficients are defined[10,26–28,37–42]

$$a^{(k)}(j, j') = [k]\,\frac{S_{qq}^{(kk)*}(j, j')}{S_{00}^{(00)}(j, j')} = \frac{\sigma^{(kk)}(j, j')}{\sigma^{(00)}(j, j')}, \tag{4}$$

where $\sigma^{(kk)}(j, j')$ are the tensor cross sections of Alexander and Davis, and Follmeg *et al.*,[26–28,37,38] while $S_{qq}^{(kk)*}(j, j')$ are the *correlation coefficients* defined by Miranda and Clary.[39] Expressions relating these coefficients to the scattering T-matrix, elements have been presented by a number of authors.[26,27,37–39]

We have shown previously that at fixed relative velocity, $v_{\rm rel}$, the bimolecular rate coefficients for collisional depolarization are given by[11,15,16]

$$\begin{aligned} k_{j\to j'}^{(k)} &= k_{j\to j'}\,[1 - a^{(k)}(j, j')] \\ &= v_{\rm rel}\,\sigma_{j\to j'}(v_{\rm rel})[1 - a^{(k)}(j, j')], \end{aligned} \tag{5}$$

where $k_{j\to j'}$ and $\sigma_{j\to j'}(v_{\rm rel})$ are the collision rate coefficients and cross sections, respectively. Note that the depolarization rate coefficients and cross sections are related by $k_{j\to j'}^{(k)} = v_{\rm rel}\sigma_{j\to j'}^{(k)}$. The quantum mechanical derivation of this expression has been presented by Dagdigian and Alexander.[26] Note that in terms of the tensor cross sections of Eq. (4), we can write the depolarization cross sections[26,27]

$$\begin{aligned} \sigma_{j\to j'}^{(k)} &= \sigma_{j\to j'}(v_{\rm rel})\,[1 - a^{(k)}(j, j')] \\ &= ([j']/[j])^{1/2}[\sigma^{(00)}(j, j') - \sigma^{(kk)}(j, j')]. \end{aligned} \tag{6}$$

If the total collision rate coefficients are known, the measurement of the depolarization rate coefficients therefore allows direct evaluation to be made of the $\boldsymbol{j}$-$\boldsymbol{j}'$ vector correlation, as quantified by the $a^{(k)}(j, j')$ expansion coefficients. From the classical definition of the polarization parameters given by Eq. (3), it is clear that $a^{(2)}(j, j')$ must lie within the limits $-\frac{1}{2} \le a^{(2)}(j, j') \le 1$, and consequently the alignment depolarization rate coefficients are bounded by $\frac{3}{2}k_{j\to j'} \ge k_{j\to j'}^{(2)} \ge 0$. Therefore, when $a^{(2)}(j, j')$ is negative, the depolarization rate coefficient can exceed the collision rate constant. Similarly, since $a^{(1)}(j, j')$ ranges classically from $-1 \le a^{(1)}(j, j') \le 1$, the orientation depolarization rate coefficients must lie between $2k_{j\to j'} \ge k_{j\to j'}^{(1)} \ge 0$. These equations provide a convenient link between the measured depolarization rate coefficients, and the dynamically interesting $\boldsymbol{j}$-$\boldsymbol{j}'$ depolarization parameters, $a^{(k)}(j, j')$. The limits on the quantum mechanical $a^{(k)}(j, j')$ parameters can differ from the values given above at low N, as has been discussed in general terms previously.[10]

The present experiments are not conducted at a well defined collision energy, and hence the measured quantities are averages over a distribution of relative velocities. The velocity averaged value of $a^{(k)}(j, j')$ can be written:[11]

$$\langle a^{(k)}(j, j')\rangle = \frac{\langle v_{\rm rel}\, \sigma_{j\to j'}(v_{\rm rel})\, a^{(k)}(j, j'; v_{\rm rel})\rangle}{\langle v_{\rm rel}\, \sigma_{j\to j'}(v_{\rm rel})\rangle}, \quad (7)$$

such that

$$\left\langle k^{(k)}_{j\to j'}\right\rangle = \langle k_{j\to j'}\rangle\,[1 - \langle a^{(k)}(j, j')\rangle]. \quad (8)$$

Finally, we can define the total depolarization rate constant for a specific initial state j as[11]

$$k^{(k)}_j(T) \equiv \left\langle k^{(k)}_j\right\rangle = \sum_{j'}\langle k_{j\to j'}\rangle\,[1 - \langle a^{(k)}(j, j')\rangle]. \quad (9)$$

A similar expression can be written for the final state averaged collision and depolarization cross sections, $\langle\sigma^{(k)}_j\rangle$. The present article focusses specifically on the depolarization cross sections with $k = 1$ and $k = 2$, representing loss of orientation and alignment, respectively. In the case of elastic depolarization, j should replace j' in the above equations. In practice, the thermally averaged cross sections presented here were obtained by dividing the measured rate coefficients by the mean relative velocity (see Sec. II B).

B. QCT method

Batches of approximately 1×10^5 trajectories were run for several initial N states at a fixed collision energy of 39 meV for both OH(A) + Kr and NO(A) + Kr. This collision energy corresponds to the mean thermal energy at 300 K. It was shown in Ref. 17 that QCT results at this fixed collision energy are in excellent agreement with those calculated using a 300 K thermal Maxwell-Boltzmann distribution of collision energies for OH(A) + Kr. The QCT method employed was similar to that described in Ref. 43, and will only be described briefly here. Since the PESs for OH(A)-Kr[17] and NO(A)-Kr[36] have only been calculated using the fixed equilibrium bond lengths of the radicals, the method of Lagrange multipliers was used to force rigid rotor behavior during the integration of the classical equations of motion. To assign the final state for each trajectory, the square of the rotational angular momentum $|\boldsymbol{N}'|^2 = N'(N'+1)\hbar^2$ was first calculated, and then the values of N' thereby obtained were rounded to the nearest integer. Trajectories for which the final N' quantum numbers were found to lie between $N \pm 0.5$ were considered elastic.

Note that the above treatment is appropriate for QCT calculations in which OH(A) + Kr and NO(A) + Kr are treated as closed shell systems. QCT evaluation of the "open shell" spin-rotation and hyperfine level changing cross sections, and the associated polarization parameters, were obtained using the tensor opacity formalism described in detail previously.[10,15]

C. TSH-QCT method

Non-adiabatic TSH-QCT calculations[44] were carried out for OH(A) + Kr with a fixed collision energy of 39 meV, using the fewest switches algorithm of Tully.[45] These calculations were performed in the same way as our previous work on this system in Ref. 35, so are described only briefly here. Trajectories were propagated on the MRCI adiabatic potential energy surfaces $2A'$ and $1A'$ described in Ref. 35. These adiabatic states are related to the diabatic states $\Sigma_{A'}$ and $\Pi_{A'}$ by an orthogonal transformation:[35]

$$\begin{pmatrix} V_{1A'} & 0 \\ 0 & V_{2A'} \end{pmatrix} = \mathbf{C}\begin{pmatrix} V_{\Pi_{A'}} & V_{\Sigma\Pi} \\ V_{\Sigma\Pi} & V_{\Sigma_{A'}} \end{pmatrix}\mathbf{C}^T, \quad (10)$$

in which

$$\mathbf{C} = \begin{pmatrix} \cos\gamma & \sin\gamma \\ -\sin\gamma & \cos\gamma \end{pmatrix}. \quad (11)$$

The kinetic coupling between these adiabatic states is given by the product of the nuclear velocities with the non-adiabatic coupling matrix elements (NACMEs), which are obtained from the derivative of the so-called *mixing angle*, γ, in Eq. (11).[35] At each time step, the populations of the electronic states $2A'$ and $1A'$ were integrated using an Adams-Bashforth-Moulton predictor-corrector algorithm, and the probability of a hop to the other potential energy surface was calculated according to the prescription in Ref. 45. After a successful hop, the momentum of each nucleus was rescaled in the direction of the non-adiabatic coupling vector in order to conserve the total energy of the system.[45,46] If the energy gap between the adiabatic potentials is larger than the translational energy of the system, the hop is rejected (a "frustrated" hop).

As reported previously,[35] a cross section for electronic quenching was calculated from the number of trajectories ending in the $1A'$ electronic state, $\mathcal{N}_{\rm Q}$:

$$\sigma_{\rm Q} = \pi b^2_{\rm max}\frac{\mathcal{N}_{\rm Q}}{\mathcal{N}_{\rm tot}} \quad (12)$$

and analysis of the trajectories that remained on the excited $2A'$ PES was carried out in the same way as in Sec. II B.

This treatment only accounts for coupling between the $2A'$ and $1A'$ adiabatic potential energy surfaces, neglecting the rotationally induced Coriolis coupling between the $2A'$ and $1A''$ states. Furthermore, note that the diabatic PES and the coupled PESs employed here are calculated with somewhat different levels of theory. The diabatic PES was calculated at the RCCSD(T) level of theory,[17] while the coupled potentials employed in the TSH-QCT calculations were determined at the MRCISD+Q level of theory.[35] As a consequence, the QCT and TSH-QCT results are slightly different, even when there is no hopping included in the latter calculation.

D. QM method

Fully quantum mechanical close-coupling scattering calculations of integral and tensor cross sections were also performed on the single-sheet, diabatic RCCSD(T) Kr-OH($A^2\Sigma$) PES[17] using the HIBRIDON suite of codes,[47] which employs a hybrid propagator comprised of the Log-Derivative propagator by Manolopoulos[48,49] and the Airy propagator for the long-range region. The Log-Derivative propagation was performed from 3 to 9 bohrs and Airy propagation to 30 bohrs,

and partial waves up to $J = 300$ were sufficient to converge the cross sections.

The rotational basis of the OH(A) molecule was set to maximum value of $N = 29$. This basis was formed using the OH(A) rotational constant of $B_0 = 16.9602\ \text{cm}^{-1}$, centrifugal distortion constants $D = 2.039 \times 10^{-3}\ \text{cm}^{-1}$ and $H = 8.71 \times 10^{-8}\ \text{cm}^{-1}$, and finally spin-rotation constant of $\gamma = 0.201\ \text{cm}^{-1}$. The reduced mass was set to 14.138 amu based on the atomic masses of the most abundant isotopes.

E. Experimental

The experimental procedures for determining depolarization cross sections from Zeeman and hyperfine quantum beat spectroscopy have been described in detail previously,[8,11–14,16] and only a brief summary will be given here. OH(X) was generated by pulsed 193 nm photodissociation of hydrogen peroxide.[50–59] H_2O_2 was flowed in a 50:50 mixture with water through the reaction chamber at a constant partial pressure of $\lesssim$2 mTorr. Translationally thermalized, electronically excited OH(A) radicals were obtained at a fixed pump-probe laser delay of $\sim$10 μs by pulsed excitation of OH(X) using the $A\,^2\Sigma^+ \leftarrow X\,^2\Pi$ transition. The latter excitation was performed with Nd:YAG (yttrium aluminum garnet) pumped dye laser probe radiation, frequency doubled to wavelengths around 308 nm (bandwidth $\approx 0.36\ \text{cm}^{-1}$ in the UV). For the total depolarization measurements, various levels of the f_1 ($j' = N' + 1/2$) and f_2 ($j' = N' - 1/2$) spin-rotation manifolds of OH(A, $v' = 0$) were excited, while the transitions used for the elastic depolarization measurements are as detailed in Table I of Ref. 14. For the notation used, see Ref. 60.

The experiments on the depolarization of NO(A) were conducted at 300 K in a slow flow of NO(X) held at a pressure of $\lesssim$1 mTorr. NO(A) was produced by pulsed Nd:YAG pumped dye laser excitation on the 0-0 band of the NO $A\,^2\Sigma^+ \leftarrow X\,^2\Pi$ transition at frequency doubled wavelengths around 226 nm. The levels $N' = 2$, 5, 7, 9, and 14 of the f_2 spin-rotation level were excited, using the $R_{22}\uparrow$ and $S_{21}\uparrow$ transitions.

The collider gas, Kr, flowed into the chamber through a separate inlet valve to allow experiments to be performed over a range of partial pressures. The $A \rightarrow X$ spontaneous fluorescence was passed through a set of polarizing optics (see below) and a monochromator, before being detected with a UV-sensitive photomultiplier. In the case of total alignment depolarization measurements, the monochromator was used with the maximum possible bandwidth ($\approx$75 Å), with the result that the measurement was essentially unresolved. However, for the total disorientation measurements it is necessary to resolve emission from either the P or R branch to obtain a quantum beat, and for the elastic measurements to record just the fluorescence from the initially populated spin-rotation level. Therefore, the monochromator was used at a higher resolution to disperse the fluorescence. For the elastic depolarization measurements on OH(A), the monochromator bandwidth was adjusted so that only emission from the initially excited level was detected.[14] The fluorescence decay traces were recorded on a digital oscilloscope and transferred to a PC for subsequent data acquisition and analysis. The response time of the system was determined to be $\lesssim$20 ns.

In all of the experiments described here the photolysis laser radiation was used without polarization. A Glan-Taylor polarizer was used to improve the polarization of the frequency doubled dye laser radiation immediately prior to entering the reaction chamber, and the purity of the polarization was determined to be better than 95% on exiting the chamber. In the case of alignment measurements, a photoelastic modulator was used to switch the probe laser linear polarization either 90° to the fluorescence detection direction or parallel to it on alternate laser shots. The polarizer used for detection was aligned parallel to the probe laser propagation axis. For the orientation measurements, the probe radiation was switched between left and right circularly polarized light on alternate laser shots using a photoelastic modulator. A quarter waveplate followed by a Glan-Taylor polarizer were placed in front of the entrance slits of the monochromator.

The Zeeman quantum beat experiments were performed in a uniform magnetic field of between 0 and 30 Gauss. The field was produced using a pair of matched Helmholtz coils, which were placed inside the reaction chamber, about 2.5 cm away from the interaction region. As in our previous work,[8,10–16] the center of the reaction chamber was screened from external magnetic fields by μ-metal shielding. The field was checked using a Hall probe, but could also be determined from the Zeeman beat frequency, since the g_F values for OH(A) and NO(A) are known quite precisely.[61–68] For the alignment experiments, the axis of the magnetic field was aligned parallel to the fluorescence detection direction[8] while in the orientation experiments the field axis was directed perpendicular to the detection axis, and to the pump laser propagation direction.[12]

F. Data fitting

The procedures used to fit the Zeeman and hyperfine quantum beat data have been described in detail previously and this material will not be repeated here.[8,11–13] In this work, hyperfine quantum beats were only used to obtain collisional disalignment data for NO(A) + Kr in the initial state $N = 2$. Both sets of alignment quantum beats were fit with an expression of the form

$$I = A\,e^{-k_p t} \times \left[1 + e^{-k_d t} \sum_F C_F \cos(2\pi\omega t + \phi)\right], \quad (13)$$

where ω is a frequency which depends on the type of experiment performed, ϕ is the phase of the beat signal, defined by the probe laser and detector polarization geometries, and A and C_F are constants defining the total intensity and the relative beat amplitudes, respectively. In the case of orientation measurements, the difference between the Zeeman quantum beat signals obtained using left and right circularly polarized light (I_L and I_R, respectively) were fit with the expression

$$C = \frac{I_L - I_R}{I_L + I_R} = e^{-k_d t} \sum_F C'_F \cos(2\pi\omega' t + \phi), \quad (14)$$

as described elsewhere.[12]

Two phenomenological first order rate coefficients, k_p and k_d, have been introduced to allow for decay of the population and the angular momentum polarization, respectively.[69,70] The rate coefficients are dependent on the concentration of the collider, and can both be expressed as sums of rate coefficients describing collision-free and collisional-induced decay processes

$$\begin{aligned} k_p &= k_0 + k_1[\mathrm{Kr}] \\ k_d &= k_2 + k_3[\mathrm{Kr}]. \end{aligned} \tag{15}$$

In the case of the total depolarization measurements, the population decay, characterized by k_p, is associated with processes that remove OH(A) or NO(A), such as fluorescence (k_0) or electronic quenching (k_1), and not with processes such as RET that occur *within* the OH(A) or NO(A) electronic state.[8,11] k_2 is associated with depolarization in the absence of krypton, which could arise, for example, from field inhomogeneities. Of particular interest to the current work is k_3 which accounts for the collisional depolarization of the radical.

It should be noted that in the case that the fluorescence from the initially populated spin-rotation state is resolved as is the case of the elastic depolarization measurements here, k_1 contains contributions from both RET and electronic quenching. This is discussed in Ref. 17. A typical OH(A) Zeeman quantum beat signal, obtained at a range of krypton pressures, is shown in Fig. 1. Corresponding hyperfine quantum beat data for NO(A) + Kr are shown in Fig. 2. We have shown previously that the beat amplitudes are well-described by LIF linestrength theory.[11,13] For each rovibronic transition, a series of between 6 and 8 fluorescence decay curves obtained as a function of collider concentration were fitted globally, using the signal amplitudes, A, the relative beat amplitudes, C_F, the phase ϕ, and the four rate coefficients as adjustable parameters. Errors were estimated using a Monte Carlo error routine described elsewhere.[71]

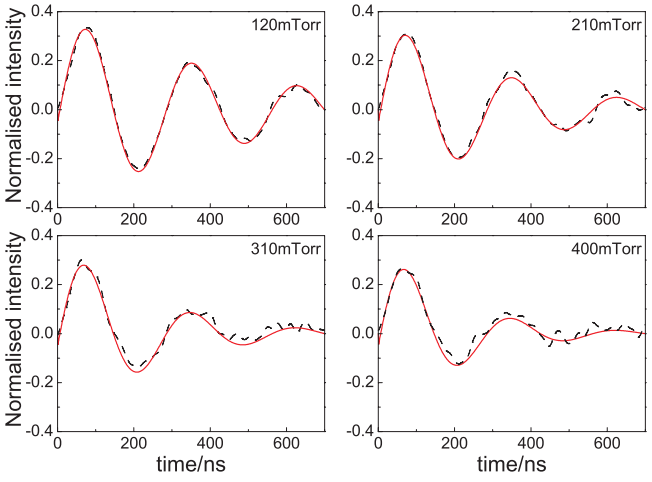

FIG. 1. A typical orientation Zeeman quantum beat for OH(A) under thermal conditions following $R_{22}(7)$ excitation (dashed line) and a fit to the data (solid line) for a range of Kr pressures. The magnetic field used was approximately 20 Gauss.

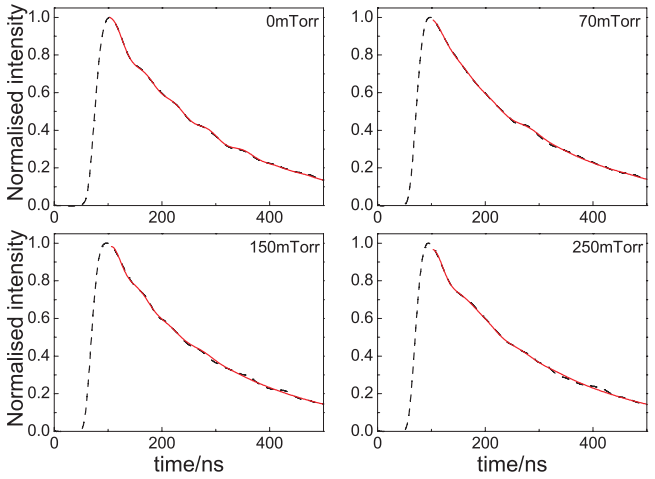

FIG. 2. A typical (thermal) alignment hyperfine quantum beat for NO(A) following $S_{21}(0)$ excitation (dashed line) and a fit to the data (solid line) for a range of Kr pressures.

III. RESULTS

A. NO(A) + Kr

A comparison of the total depolarization cross sections obtained experimentally (filled squares) and from the QCT calculations (open circles) for NO(A) + Kr is presented in Fig. 3 and Table I. All the data are for the initial f_2 ($j = N - 1/2$) spin-rotation level. These cross sections represent the sum of the contributions to depolarization arising from elastic and inelastic (RET) collisions.[11] The left hand panels show the disorientation cross sections and the right hand panel the disalignment cross sections. The agreement between the two sets of results for both the orientation and alignment data is very good.

In Fig. 3, the results from experimental simulations are also shown (open triangles). These simulations allow for the effects of dephasing, which is indistinguishable from depolarization experimentally.[8,11,13] As input to the simulations we include the complete RET matrix from the QCT calculations and all elastic and inelastic depolarization cross sections.[11,13] Dephasing occurs because each hyperfine level of the radical has a different value of g_F. Therefore, when different hyperfine levels are populated after the collision, the radical will precess at a slightly different frequency in the applied

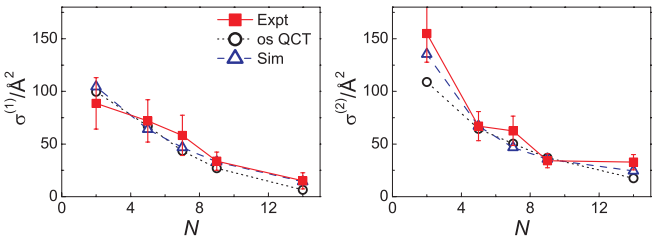

FIG. 3. Comparison of the experimentally determined *total thermal depolarization* cross sections as a function of the initial rotational level, N, for NO(A) + Kr (filled squares) with those from QCT calculations (open circles) and experimental simulations (open triangles) for disorientation (left panel) and disalignment (right panel). The data are for the f_2 ($j = N - 1/2$) spin-rotation level.

TABLE I. Cross sections for collisional disorientation ($\sigma^{(1)}$/Å^2) and disalignment ($\sigma^{(2)}$/Å^2) of NO(A) by Kr under thermal conditions. The QCT calculations were performed at a collision energy of 39 meV. The error bars (indicated in brackets on the experimental data) were determined using a Monte Carlo procedure,[71] and represent 95% confidence limits. All the data are for the f_2 ($j = N - S$) spin-rotation level. The experimental simulation results are explained in more detail in Sec. III.

		$N = 2$	$N = 5$	$N = 7$	$N = 9$	$N = 14$
$\sigma^{(1)}$	Experiment	89(24)	72(20)	58(19)	34(9)	15(8)
	QCT	99.7	66.9	43.4	27.1	6.5
	Simulation	104.4	63.9	46.7	33.1	14.2
$\sigma^{(2)}$	Experiment	155(27)	67(14)	63(14)	34(7)	33(7)
	QCT	108.8	64.4	50.3	37.0	17.5
	Simulation	135.3	67.0	46.8	35.6	24.5

magnetic field. The total recorded signal is, therefore, a sum of many beat signals with slightly different frequencies, which leads to a loss of the beat even in the absence of depolarization. The importance of dephasing depends on the extent to which collisions populate different final states. Spin-rotation state changing collisions ($\Delta N \neq \Delta j \neq 0$) contribute most to the dephasing effect, as such collisions lead to population of a quantum state in which the direction of precession is reversed compared with that for the state initially excited. Collisions that change N but conserve S (and nuclear spin, I) contribute less, as the g_F values for consecutive N states do not change significantly. The largest difference between neighbouring states occurs at low N, meaning that dephasing will be most significant at low N.

As can be seen from Fig. 3, the inclusion of dephasing effects, which are quite modest in this case, leads to excellent agreement between the experimental and theoretical results for NO(A) + Kr, both for disorientation and disalignment.

B. OH(A) + Kr

1. Rotational energy transfer

RET cross sections have been measured for a range of rotational states in both spin-rotation levels, and are shown in Fig. 4.[17] The range of experimentally accessible states is limited by the resolution of the monochromator (maximum ~1 Å). The results shown are an extension of the data set reported in our previous work.[17] The experimental results are compared to the QCT and QM calculations performed on the single OH(A) + Kr diabatic RCCSD(T) PES[17], and with the new TSH-QCT calculations on the MRCISD+Q PESs.[35]

There is excellent agreement between the experimental and theoretical RET cross sections, both for the single surface[17] and the non-adiabatic TSH-QCT calculations. The single surface QCT calculations predict a smooth decrease in RET cross sections with increasing N above $N = 4$, a trend that is reflected in the experimental data. However, below this N value, in the region where quenching is most significant, the experimentally observed RET cross sections are somewhat lower than predicted by the single surface calculations. The TSH-QCT data can be seen to replicate better the experimental results at low N, while remaining in close agreement with single surface QCT at higher N.

As noted in Sec. II C, electronic quenching is assumed to occur through crossing between the two diabatic PES's of A′ reflection symmetry. Quenching takes place in the region of the PESs at which non-adiabatic coupling is highest—near the bottom of the deeper, HO–Kr well, close to the global minimum of the excited state PES (see Figs. 6 and 7 of Ref. 35). This is also the region where the potential is the most anisotropic, leading to the most rotational energy transfer. Including non-adiabatic effects in the calculations means that molecules experiencing this part of the potential are less likely to remain on the excited state PES, and so the effect of

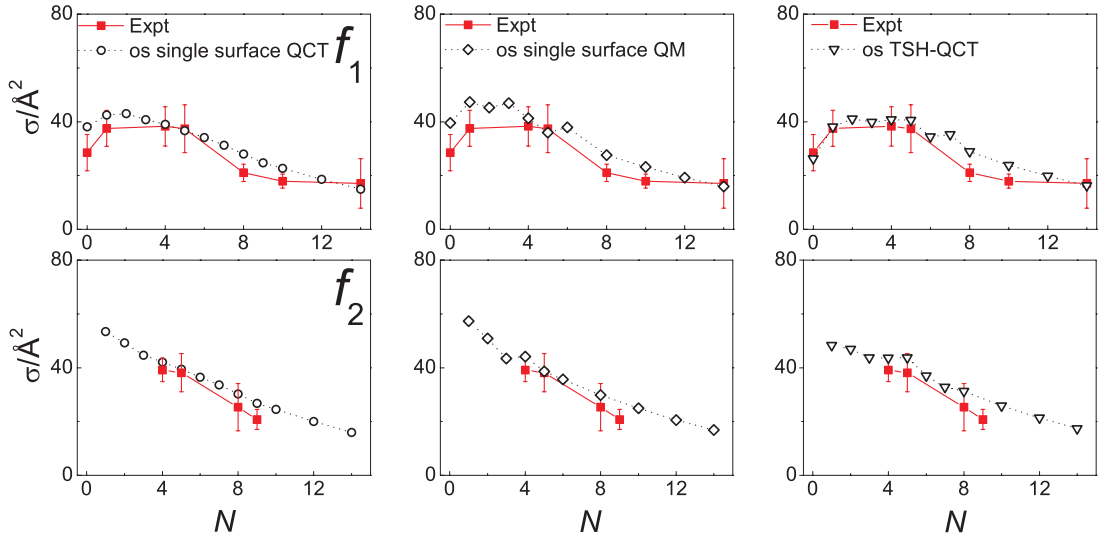

FIG. 4. Comparison of the experimental (filled red squares) and theoretical open shell (os) thermal RET cross sections as a function of the initial N state for OH(A) + Kr. Left column: single surface QCT (black open circles). Middle column: single surface QM (black open diamonds). Right column: non-adiabatic TSH-QCT (black open triangles). The upper panels show the cross sections for the f_1 spin-rotation level ($j = N + 1/2$), and the lower panels show the f_2 spin-rotation level ($j = N - 1/2$). All of the calculations were performed at a fixed collision energy of $E_{coll} = 39$ meV.

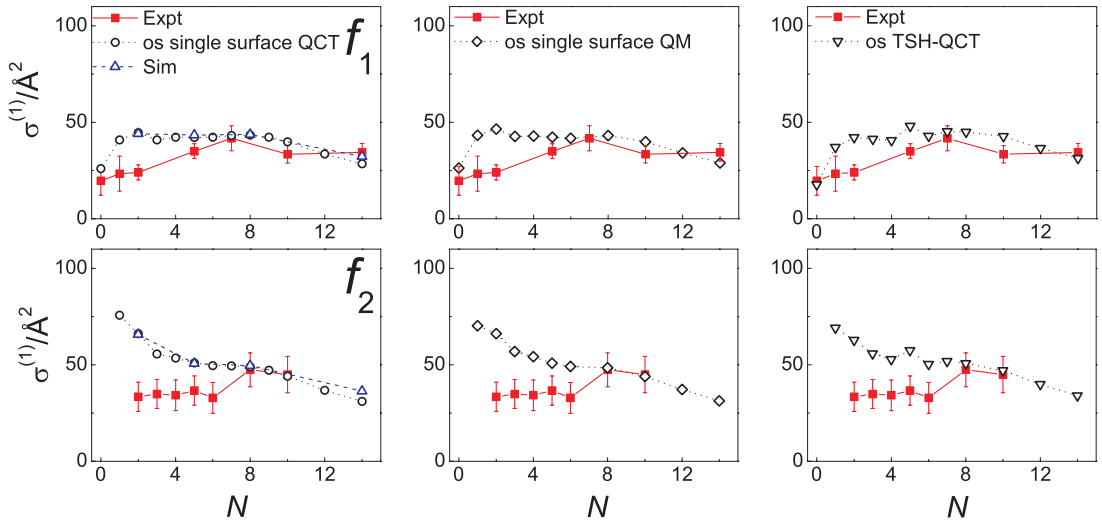

FIG. 5. Comparison of the experimentally determined *total (elastic + inelastic) thermal disorientation* cross sections for OH(A) + Kr (filled squares) with those from theoretical open shell (os) calculations for the f_1 (top panels) and f_2 (bottom panels) spin-rotation levels. The left hand panels present the results from the single surface QCT calculations (open circles), and the middle panels present the QM results (open diamonds). The right hand panels show results from the surface-hopping QCT calculations. All of the calculations were performed at a fixed collision energy of $E_{coll} = 39$ meV.

quenching is to reduce the RET cross section to some extent, mainly for low rotational states, as observed in the TSH-QCT calculations. This reduction is, however, relatively small, because the cross sections for RET are about a factor of 3-4 larger than the total quenching cross sections at low N, and beyond $N = 9$ quenching is almost negligible (see Fig. 2 of Ref. 35). With increasing N, the OH(A) rotational motion becomes increasingly fast in comparison to OH(A) + Kr translation, to the point that the incoming Kr atom no longer "sees" the region of non-adiabatic mixing.

2. Total depolarization

The experimentally measured total (elastic plus inelastic) disorientation and disalignment cross sections recorded for OH(A) + Kr under thermal conditions are shown in Figs. 5 and 6, respectively, where they are compared with the results from single surface QCT (left panels), single surface QM (middle panels), and TSH-QCT (right panels) calculations. The results are also presented in Tables II and III. Neither the disorientation nor the disalignment experimental data agree with theoretical calculations as well as in the case of NO(A) + Kr. Clearly, the calculations fail to capture the unusual trend in the depolarization cross sections with N. This is somewhat surprising given the good agreement between the QCT, TSH-QCT, and experimental RET cross sections presented in Fig. 4. Note that the results from the single surface QCT calculations agree well with the single surface QM calculations, indicating that the discrepancy between experiment and single surface theory is not a reflection of quantum features that are not accounted for in the QCT method.

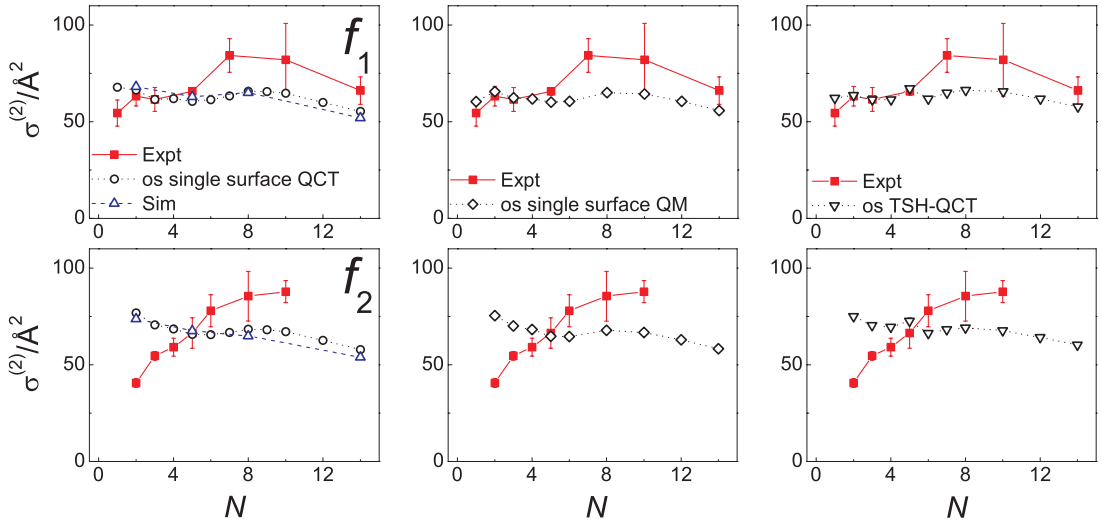

FIG. 6. Same as Fig. 5 but showing the *total (elastic + inelastic) thermal disalignment* cross sections. The simulations are shown in the left panels as blue upwards-pointing open triangles.

TABLE II. Cross sections for collisional disorientation ($\sigma^{(1)}$/Å^2) and disalignment ($\sigma^{(2)}$/Å^2) of OH(A) by Kr under thermal conditions, for f_1 ($N + S$) spin-rotation levels. The single surface QCT, single surface QM, and surface-hopping TSH calculations were performed at a collision energy of 39 meV. The error bars (indicated in brackets on the experimental data) were determined using a Monte Carlo procedure,[71] and represent 95% confidence limits.

f_1	$N=$	0	1	2	3	4	5	6	7	8	10	12	14
$\sigma^{(1)}$	Expt. total	20(7)	23(9)	24(4)	…	…	35(4)	…	42(7)	…	33(5)	…	34(5)
	Expt. elastic	0(14)	3(14)	…	…	…	…	…	…	…	…	…	23(7)
	QCT total	26	41	45	41	42	42	42	43	43	40	34	28
	QCT elastic	0	11	12	11	12	13	14	16	18	20	19	18
	QM total	26	43	47	43	43	42	42	…	43	40	34	29
	QM elastic	0	9	11	11	11	13	13	…	18	19	19	18
	TSH total	18	37	42	41	41	48	43	45	45	43	36	31
	TSH elastic	0	10	11	11	11	15	14	16	18	20	20	19
$\sigma^{(2)}$	Expt. total	…	54(7)	63(5)	62(6)	…	66(2)	…	84(9)	…	82(19)	…	66(7)
	Expt. elastic	…	22(12)	23(11)	…	28(11)	20(7)	…	…	…	…	…	32(13)
	QCT total	…	68	67	62	62	60	61	63	66	65	60	55
	QCT elastic	…	26	25	23	25	26	28	31	34	37	38	37
	QM total	…	60	66	62	62	60	61	…	65	64	61	56
	QM elastic	…	19	23	22	23	26	26	…	34	37	37	37
	TSH total	…	62	64	61	61	67	62	65	66	66	62	58
	TSH elastic	…	25	25	24	24	30	28	31	34	37	38	38

The right hand panels of Fig. 5 compare the experimental disorientation cross sections to the results of the non-adiabatic TSH-QCT calculations. In effect, the most depolarizing trajectories from the single surface calculations are "lost" to electronic quenching in the deep well of the OH(A)–Kr PES, thus reducing the calculated depolarization cross sections. This is mostly evident at low values of N, where the quenching cross sections are highest.[34,35] As N increases, and the electronic quenching cross sections fall,[35] the experimental and QCT depolarization cross sections display better agreement.

It can be seen in Fig. 5 that the decrease in the TSH-QCT disorientation cross sections relative to those from the single surface QCT calculations on the $2A'$ PES leads to slightly improved agreement with experiment. However, the change in depolarization cross section is not sufficient to fully explain the disagreement with experiment. In Ref. 35, it was seen that, except for $N = 0$, 1, the TSH-QCT method also underestimates the experimental electronic quenching cross sections. As discussed more in Sec. IV, if the theoretical TSH-QCT quenching cross sections matched experiment better, it is likely that this would yield calculated depolarization cross sections that were smaller, improving the agreement with the data shown here.

Similar comments hold for the comparison between experimental and theoretical total disalignment cross sections shown in Fig. 6. The results for f_1 states are in somewhat better agreement with the theoretical data than those corresponding to initial f_2 states. However, the discrepancies in both cases are remarkable for $N > 5$ in contrast with the

TABLE III. Cross sections for collisional disorientation ($\sigma^{(1)}$/Å^2) and disalignment ($\sigma^{(2)}$/Å^2) of OH(A) by Kr under thermal conditions, for f_2 ($N - S$) spin-rotation levels. The single surface QCT, single surface QM, and surface-hopping TSH calculations were performed at a collision energy of 39 meV. The error bars (indicated in brackets on the experimental data) were determined using a Monte Carlo procedure,[71] and represent 95% confidence limits.

f_2	$N=$	1	2	3	4	5	6	7	8	10	12	14
$\sigma^{(1)}$	Expt. total	…	33(8)	35(8)	34(8)	37(8)	33(8)	…	47(9)	45(9)	…	…
	Expt. elastic	…	11(3)	…	9(7)	10(7)	…	…	27(8)	…	…	…
	QCT total	76	66	56	54	51	50	50	49	44	37	31
	QCT elastic	19	16	15	15	15	16	18	20	22	21	20
	QM total	70	66	57	54	51	49	…	49	44	37	31
	QM elastic	6	15	14	14	15	15	…	20	21	21	19
	TSH total	69	63	56	53	58	50	52	51	47	40	34
	TSH elastic	18	16	15	14	18	17	19	20	22	22	21
$\sigma^{(2)}$	Expt. total	…	41(2)	55(2)	59(5)	67(8)	78(8)	…	86(13)	88(6)	…	…
	Expt. elastic	…	21(12)	…	32(12)	18(12)	…	…	45(15)	…	…	…
	QCT total	…	77	71	69	66	66	67	68	67	63	58
	QCT elastic	…	27	26	26	27	28	31	34	37	38	39
	QM total	…	76	70	68	65	65	…	68	67	63	58
	QM elastic	…	24	23	24	26	26	…	34	37	37	37
	TSH total	…	75	70	70	73	66	68	69	68	64	60
	TSH elastic	…	27	27	26	31	29	31	34	37	38	39

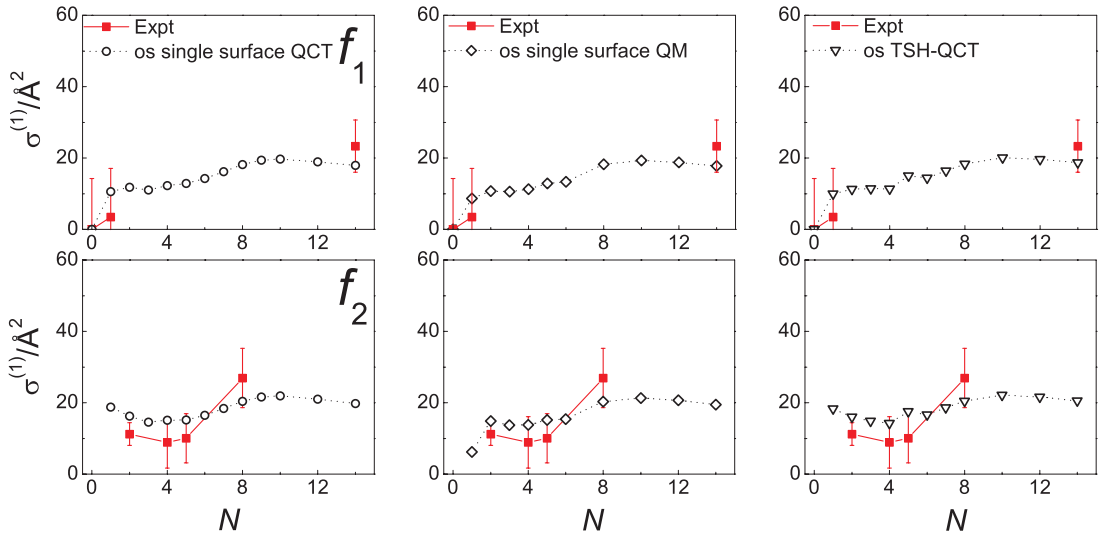

FIG. 7. Comparison of the experimentally determined *elastic thermal disorientation* cross sections for OH(A) + Kr (filled squares) with those from theoretical open shell (os) calculations for f_1 levels (top panels) and f_2 levels (bottom panels). The left hand panels present the results from the single surface QCT calculations (open circles), and the middle panels present the QM results (open diamonds). The right hand panels show the surface-hopping QCT results. All of the calculations were performed at a fixed collision energy of $E_{\text{coll}} = 39$ meV.

results for disorientation cross sections for which there seem to be a better accordance for the high N values.

To discard the possibility that dephasing could cause the observed discrepancies, simulations of the experiment have also been performed for OH(A) + Kr at the same collision energy (shown in the figures as upwards triangles). As for NO(A) + Kr, we take the single surface QCT theoretical data as input to these simulations, although very similar results were obtained if the TSH-QCT results were employed. The results are indistinguishable from the open shell QCT calculations, showing that dephasing does not contribute to the depolarization cross sections. Under thermal conditions, collisions between OH(A) and Kr cause complete depolarization. Therefore, the states populated after the collision are effectively unpolarized, and will not contribute to the polarization signal.

3. Elastic depolarization

The experimentally determined elastic depolarization cross sections recorded for OH(A) + Kr under thermal conditions are compared with the results from theoretical calculations in Figs. 7 and 8 for disorientation and disalignment, respectively. The data were acquired for f_1 and f_2 spin-rotation states, as specified in Tables II and III. The results from the single surface QCT calculations are shown in the left hand panels, the QM results are presented in the middle panels, and TSH-QCT results are shown in the right hand panels. There is good agreement between the experiment and theory, although both the QM and QCT calculations appear to show somewhat less of a dependence on N than the experimental data. The elastic depolarization cross sections appear to increase with N, a point that will be discussed further in Sec. IV. It should

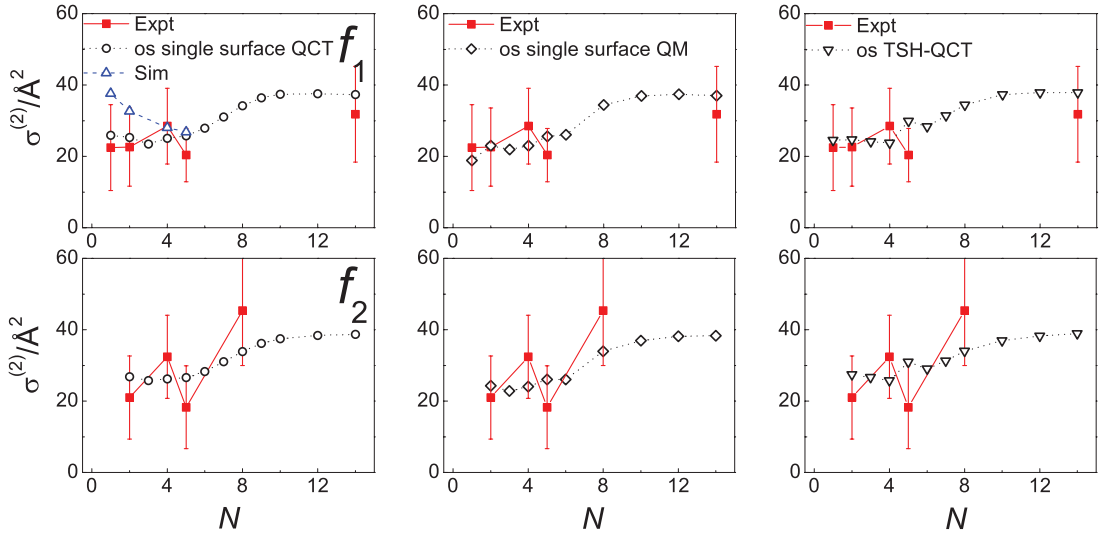

FIG. 8. Same as Fig. 7 but showing the *elastic thermal disalignment* cross sections. The simulations are shown in the upper left panel as blue upwards-pointing open triangles.

be noted that the value of $\sigma^{(1)}$ for the f_1 level with $N = 0$ is zero within the errors of the experiment. The only contribution to this state is the electron and nuclear spin of the radical, the direction of which cannot be readily altered by collision. The fact that the collisional depolarization cross section for this state is close to zero confirms that electron and nuclear spin can be treated as spectators to the dynamics.

In the case of alignment, it was necessary to run simulations of the experiment for the low N, f_1 levels, for which Q branch emission was recorded. The results from these are presented in Fig. 8 as open upward triangles. The simulations were necessary as the resolution of the experiment was insufficient to resolve the emission from just the initially populated j level. This means the satellite emission from the other j level in the initially populated N level contributed to the signal. Population of this state corresponds to a pure spin-rotation level changing collision, and is likely to cause significant dephasing because the g_F value changes sign, causing the radical to precess in the opposite direction. It should be noted that the f_2 data and the $N = 14, f_1$ data were recorded using P branch emission to allow resolution of only the initially populated j level. Including the effects of emission from the satellite lines significantly affects only the theoretical values of the cross sections for the $N = 1$ and $N = 2$ levels. The g_F values vary most quickly at low N, suggesting that the dephasing effect will be most significant for these levels. Including this effect results in the theoretical disalignment cross sections somewhat overestimating the experimental values at low N.

4. *Inelastic depolarization*

Given that both the total depolarization cross sections and elastic depolarization cross sections have been measured experimentally, it is possible to determine an experimental value for the inelastic depolarization cross sections under thermal conditions. These are presented as filled squares in Figs. 9 and 10 for disorientation and disalignment, respectively, alongside the results from the single surface QCT and QM calculations in the left and middle panels. As expected from the previous data, there is disagreement between the experimental and theoretical values, with the theoretical values falling more quickly with N than those determined experimentally. The largest discrepancy between the two sets of results is at low N. For low rotational levels, the krypton will experience the full anisotropy of the PES, whereas at higher N the faster rotation of the radical means the potential sampled during collision will be more isotropic. Therefore, the potential well will play a more significant role at low N. Any inaccuracies in the attractive part of the PES, or indeed the neglect of electronic quenching in regions of the potential wells, will consequently be magnified at low N, and could contribute to the observed disagreement between the experimental and theoretical depolarization cross sections. The fact that the agreement between the experimental and theoretical elastic depolarization cross sections is good, while there are substantial differences in the comparison for the total depolarization cross sections, clearly indicates that the main differences between the two sets of results can be attributed to the inelastic depolarization cross sections, as clearly shown in Figs. 9 and 10.

Note that the TSH-QCT inelastic depolarization cross sections, also shown in right hand panels of Figs. 9 and 10, are very slightly smaller than the single surface QCT results at low N, but remain in poor agreement with the experimental results, particularly for the f_2 spin-rotation states.

IV. DISCUSSION

A. Role of elastic depolarization

Figure 11 shows the disorientation (top panels) and disalignment (bottom panels) cross sections for OH(A) + Kr (left and middle panels) and for NO(A) + Kr (right panels) recorded under thermal conditions. The comparison between

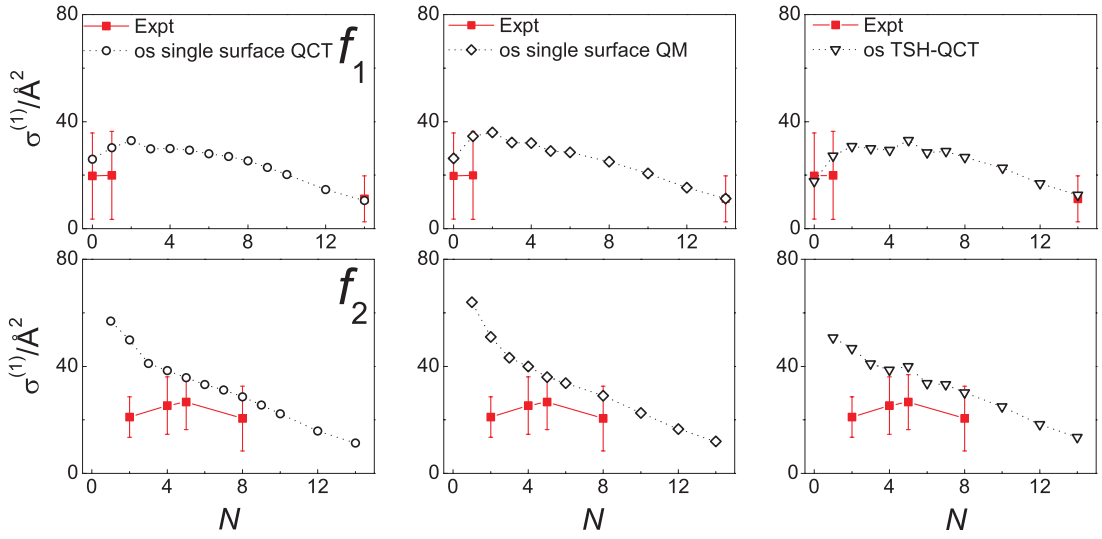

FIG. 9. Comparison of the *inelastic thermal disorientation* cross sections determined by subtracting the experimental elastic disorientation cross section from the experimental total disorientation cross sections (see Tables II and III—filled squares), and those obtained from the open shell (os) single surface QCT calculations (open circles—left panels), the single surface QM calculations (open diamonds—middle panels), and TSH-QCT calculations (open triangles—right panels). Cross-sections for the f_1 spin-rotation level are shown in top row, and for the f_2 spin-rotation level in the bottom row. All of the calculations were performed at a fixed collision energy of $E_{coll} = 39$ meV.

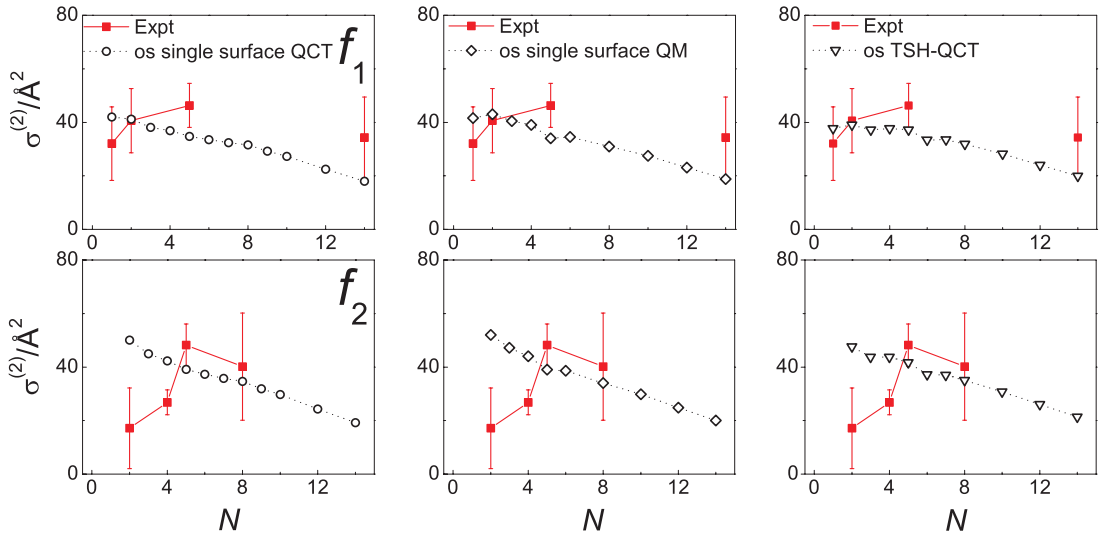

FIG. 10. Same as Fig. 9 but showing the *inelastic thermal disalignment* cross sections.

the experimentally determined total depolarization cross sections (filled squares) and the OH(A) + Kr elastic depolarization cross sections (open squares) is shown in the figure. In the case of the NO(A) + Kr, elastic depolarization cross sections could not be measured and were obtained from QCT calculations (open circles). As clearly evinced by Fig. 11, elastic depolarization plays a much more important role for OH(A) + Kr than for NO(A) + Kr. This reflects in part the much deeper wells in the PES for OH(A) + Kr, and partly the significantly greater rotational energy level spacing in OH(A) compared to NO(A), due to the different reduced masses of the two radicals.

The trend in the total and elastic depolarization cross sections is also different in the two radicals, with the cross sections falling with N in NO(A) + Kr, and increasing with N for OH(A) + Kr before falling past $N = 10$. However, the trends in the elastic depolarization cross sections are mirrored in the trend in the total depolarization cross sections in both cases. As has been discussed previously,[14,26,27] efficient elastic depolarization is caused by "following" type trajectories, where the anisotropy of the PES is sufficient for the radical to trap the krypton in a complex. At higher N, the rotation of the radical will reduce the anisotropy of the PES, and the potential the Kr experiences will be partially averaged over the attractive ends of the radical and the repulsive T-shaped geometries. Even at the highest N in the current study, there is significant elastic depolarization for OH(A) + Kr, showing the faster rotation is insufficient to "wash out" the anisotropy of the PES, and orbiting or following type trajectories can still occur. In contrast, the significantly less attractive interaction between NO(A) and Kr does not lead to orbiting trajectories at any N. Therefore, the collisions are entirely impulsive and the elastic depolarization cross sections fall with N.

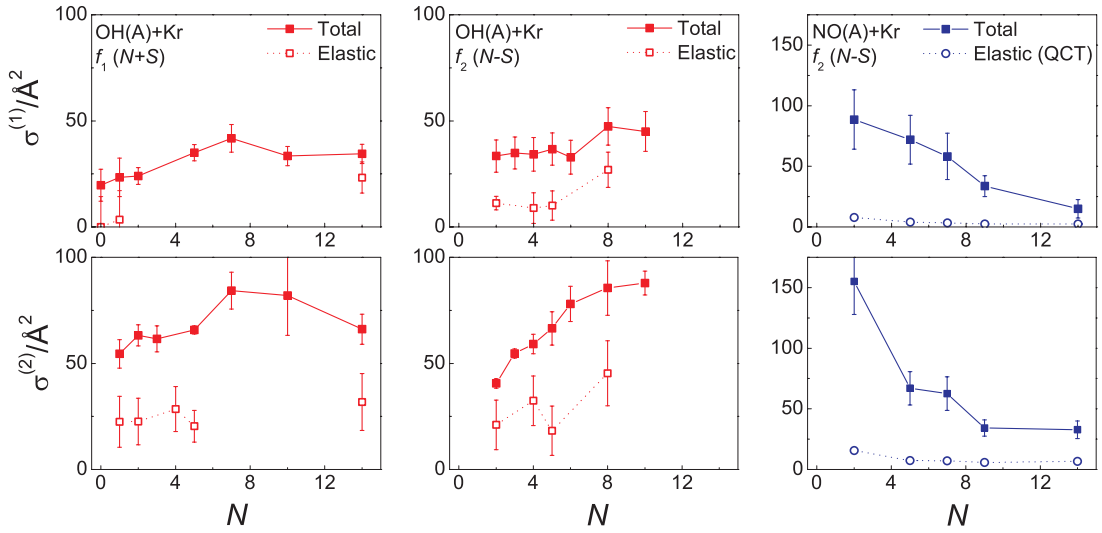

FIG. 11. Comparison of the *total thermal depolarization* cross sections (filled squares) with the *elastic thermal depolarization* cross sections (open squares) measured experimentally under thermal conditions for OH-Kr (left hand panels: f_1 spin-rotation level, middle panels: f_2 spin-rotation level), and the total (thermal) experimental (filled squares) and theoretical elastic depolarization cross sections (open circles) for NO-Kr (right hand panels). The top panels correspond to disorientation, and the bottom panels correspond to disalignment. All of the calculations were performed at a fixed collision energy of $E_{\text{coll}} = 39$ meV.

B. Experiment versus theory

As mentioned in Sec. III, while there is an excellent agreement between the NO(A) + Kr experimental and (single surface) theoretical depolarization cross sections (see Fig. 3), this is not the case for OH(A) + Kr, particularly for the f_2 spin-rotation levels. It is proposed that the main reason for the discrepancy between experiment and theory is the effect of electronic quenching in the OH(A) + Kr system. This leads to a significant loss of population of the excited state in OH(A) + Kr, whereas it can be neglected in NO(A) + Rg and OH(A) + He/Ar. As shown previously,[17,34,35] the electronic quenching cross sections decrease rapidly as N increases. The agreement between the QCT theoretical and experimental depolarization cross sections is generally observed to be better at higher N, for which electronic quenching is less significant and can be neglected (as has been the case in previous studies). This suggests that the presence of electronic quenching at lower N may be responsible for the discrepancy between the experiment and single surface QCT calculations. Electronic quenching takes place near the most attractive and anisotropic region of the OH(A) + Kr PES, the near-linear HO(A)–Kr well,[35] precisely the region of the PES that is responsible for the most depolarization. Adiabatic trajectories that experience these regions of the potential contribute a large amount to the QCT depolarization cross sections, but in reality will be quenched and end up on the $1A'$ PES.

TSH-QCT calculations have been performed in an attempt to account for the effects of electronic quenching. Indeed, the TSH-QCT depolarization cross sections display somewhat better agreement with experiment, although the improvement is not enough to fully explain the experimental results. A reason for this can be seen by examining the TSH-QCT quenching cross sections recently reported in Ref. 35. The TSH-QCT calculations capture the trend in the electronic quenching cross section as a function of the initial rotational quantum number, $\sigma_Q(N)$, but predict a much faster decay of $\sigma_Q(N)$ with N than that observed experimentally. Hence, not surprisingly, the TSH-QCT theory fails in lowering the single surface calculated depolarization cross section sufficiently to bring it into accordance with the experimental data. Clearly, both manifestations of the non-adiabaticity of the process, quenching to the ground state and the associated decrease of the depolarization cross sections, are not fully explained. Including Coriolis coupling between the $2A'$ and $1A''$ PESs in the TSH-QCT theory could increase the extent of quenching, thus reducing the calculated depolarization cross sections and improving the agreement with experiment. A full quantum dynamical treatment of the electronic quenching process would clearly be desirable. Further improvements to the PESs and the couplings between them may also be required to bring experiment into quantitative agreement with experiment.

Separating out the contributions that elastic and inelastic depolarization make to the total depolarization reveals that the main discrepancy between experiment and theory is in the inelastic depolarization cross sections. Efficient quenching will occur in the deep HO(A)–Kr potential well, but this attractive well is also likely to be most effective at inducing inelastic depolarization. Because elastic depolarization does not appear to compete with electronic quenching in the same way as inelastic depolarization does, and is predicted adequately by the single surface QCT calculations, it appears that elastic depolarizing collisions are not so dependent on the specific region of the OH(A)–Kr PES at which inelastic and quenching collisions take place.

Figure 12 displays opacity functions from TSH-QCT calculations for inelastic collisions, collisions leading to quenching and collisions leading to elastic disalignment for OH(A)–Kr. For the purposes of this figure, OH(A) is treated as a closed-shell species, for which "elastic" implies $N' = N$. The depolarization opacity function is calculated *via*

$$P^{(2)}(b) = P(b)\left(1 - a^{(2)}_{NN'}(b)\right). \tag{16}$$

Note that $P^{(2)}(b)$ can be converged for elastic collisions in a QCT calculation, while $P(b)$ cannot, because in regions of large b where the conventional opacity function is not converged the depolarization parameters in Eq. (16), $a^{(2)}_{NN'}(b)$, tend to unity.[15]

The range of impact parameters required to bring about electronic quenching is seen to be similar to that required to cause an inelastic collision, supporting the idea that, at least in the QCT calculations, similar regions or features of the PES give rise to these competing processes. The presence of electronic quenching thus suppresses the cross sections for RET and inelastic depolarization. On the other hand, elastic depolarization is possible at longer range than either electronic quenching or inelastic collisions, which is consistent with

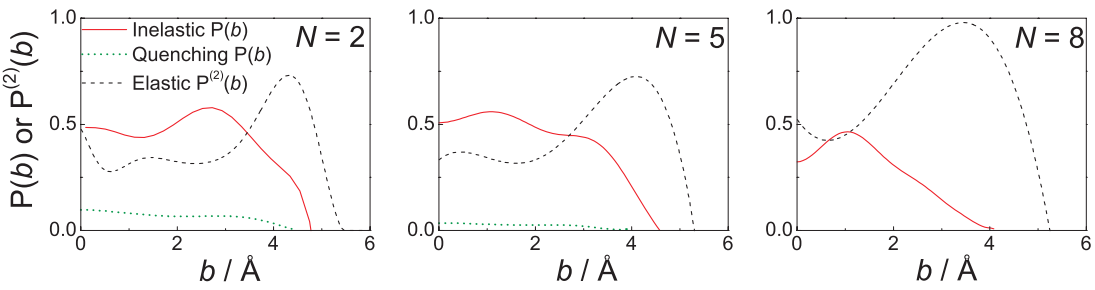

FIG. 12. Closed shell TSH-QCT opacity functions, $P(b)$ and $P^{(2)}(b)$ for OH(A) + Kr, for the initial rotational states $N = 2$, 8, and 14. Red continuous line: inelastic collisions; dotted green line: collisions leading to surface-hopping; and black dashed line: collisions leading to elastic disalignment. Note that significant surface-hopping is only predicted to occur for $N = 2$ in the TSH-QCT calculations. All of the calculations were performed at a fixed collision energy of E_{coll} = 39 meV.

these elastic depolarizing collisions taking place on a different region of the potential—most likely the longer-range OH(A)–Kr well. As these collisions do not compete with electronic quenching to the same extent as inelastic collisions do, there will be less of a discrepancy between single surface theory and experimental results for the elastic depolarization cross sections.

Another possible reason for the discrepancy between experiment and theory could be the assumption that the bond length of the radical is fixed at its equilibrium value during collision. This approximation has been used previously for NO(A) with He and Ar[13] and with OH(A) and Ar.[11,15,16] For NO(A) + He/Ar, there is good agreement between the theoretical and experimental depolarization cross sections. Similar levels of agreement are also observed in OH(A) + Ar under thermal conditions and superthermal collision energies.[16] The potential wells in the NO(A)-Rg systems are <150 cm^{-1} and in OH(A)-Ar is $\approx$1700 cm^{-1}.[9] Under these conditions, the approximation of a fixed radical bond length still appears to be valid. In these systems, it would appear that vibration is fast enough to average out any possible changes of the PES with the O–H internuclear distances, especially at low collision energies. However, the well depth for OH(A)-Kr is $\approx$6000 cm^{-1}.[17] Therefore, the OH(A) bond length is more likely to be perturbed when the krypton samples the attractive part of the PES. In addition to the effects of electronic quenching on RET and depolarization, the validity of a fixed OH bond length is something that might need to be considered in future theoretical treatments of the OH(A) + Kr system.

V. CONCLUSIONS

Quantum beat spectroscopy has been used to study the collisional disorientation and disalignment of OH(A) and NO(A) with Kr. Total depolarization cross sections have been presented for OH(A) + Kr and NO(A) + Kr under thermal (300 K) conditions. The experimental results agree well with theory for NO(A) + Kr, where the depolarization cross sections have been shown to fall with N. However, this agreement between experiment and theory is not observed for OH(A) + Kr, where the total thermal depolarization cross sections exhibit less of a dependence on N. This N-dependence has been attributed to the importance of elastic depolarization under thermal conditions in OH(A), which has also been measured experimentally, and the anisotropy of the OH(A) + Kr PES. Discrepancies between theory and experiment for OH(A) + Kr are believed to arise from the competition between electronic quenching and collisional (inelastic) depolarization, which is not accounted for in the single surface theory. Surface-hopping QCT results in improved agreement with experiment, although the underestimation of the extent of quenching in the system leads to a failure to quantitatively simulate the experimentally observed results. The inclusion of the rotation mediated Coriolis coupling between the $2A'$ and $1A''$ PES is likely to improve the agreement between theoretical and experimental results. Work is in progress in this direction.

Finally, it is worth mentioning that at higher (superthermal) collision energies, at which the electronic quenching cross sections are likely to be significantly smaller,[72,73] the agreement between the experiment and the theory improves although still the theoretical values overestimate the depolarization cross sections observed experimentally.

ACKNOWLEDGMENTS

The support of the UK EPSRC (to M.B. via Programme Grant No. EP/G00224X/1), the EU (to M.B. via FP7 EU People ITN project 238671), and the Spanish Ministry of Science and Innovation (Grant Nos. CTQ2008-02578/BQU, CSD2009-00038, and CTQ2012-37404-C02) are gratefully acknowledged. J.K. and M.H.A. acknowledge financial support from the US National Science Foundation (Grant No. CHE-1213332 to Professor M.H. Alexander).

[1] R. N. Zare, *Angular Momentum, Understanding Spatial Aspects in Chemistry and Physics* (John Wiley and Sons, 1988).
[2] K. Blum, *Density Matrix Theory and Applications* (Plenum Press, New York, 2000).
[3] E. A. Brinkman and D. R. Crosley, J. Phys. Chem. A **108**, 8084 (2004).
[4] C. H. Greene and R. N. Zare, Annu. Rev. Phys. Chem. **33**, 119 (1982).
[5] A. J. Orr-Ewing and R. N. Zare, Annu. Rev. Phys. Chem. **45**, 315 (1994).
[6] R. N. Dixon, J. Chem. Phys. **85**, 1866 (1986).
[7] U. Fano and J. H. Macek, Rev. Mod. Phys. **45**, 553 (1973).
[8] M. Brouard, A. Bryant, I. Burak, F. Quadrini, I. A. Garcia, and C. Vallance, Mol. Phys. **103**, 1693 (2005).
[9] J. Kłos, M. H. Alexander, M. Brouard, C. J. Eyles, and F. J. Aoiz, J. Chem. Phys. **129**, 054301 (2008).
[10] F. J. Aoiz, M. Brouard, C. J. Eyles, J. Kłos, and M. P. de Miranda, J. Chem. Phys. **130**, 044305 (2009).
[11] M. Brouard, A. Bryant, Y.-P. Chang, R. Cireasa, C. J. Eyles, A. M. Green, S. Marinakis, F. J. Aoiz, and J. Kłos, J. Chem. Phys. **130**, 044306 (2009).
[12] M. Brouard, H. Chadwick, Y.-P. Chang, R. Cireasa, and C. J. Eyles, Phys. Scr. **80**, 048120 (2009).
[13] M. Brouard, H. Chadwick, Y.-P. Chang, R. Cireasa, C. J. Eyles, A. O. L. Via, N. Screen, F. J. Aoiz, and J. Kłos, J. Chem. Phys. **131**, 104307 (2009).
[14] M. Costen, R. Livingstone, K. McKendrick, G. Paterson, M. Brouard, H. Chadwick, Y.-P. Chang, C. J. Eyles, F. Aoiz, and J. Kłos, J. Phys. Chem. A **113**, 15156 (2009).
[15] M. Brouard, H. Chadwick, C. J. Eyles, F. J. Aoiz, and J. Kłos, J. Chem. Phys. **135**, 084305 (2011).
[16] M. Brouard, H. Chadwick, Y.-P. Chang, C. J. Eyles, F. J. Aoiz, and J. Kłos, J. Chem. Phys. **135**, 084306 (2011).
[17] H. Chadwick, M. Brouard, Y.-P. Chang, C. J. Eyles, T. Perkins, S. A. Seamons, J. Kłos, M. H. Alexander, and F. J. Aoiz, J. Chem. Phys. **137**, 154305 (2012).
[18] H. J. Crichton, M. L. Costen, and K. G. McKendrick, J. Chem. Phys. **119**, 9461 (2003).
[19] M. L. Costen, H. J. Crichton, and K. G. McKendrick, J. Chem. Phys. **120**, 7910 (2004).
[20] S. Marinakis, G. Paterson, J. Kłos, M. L. Costen, and K. G. McKendrick, Phys. Chem. Chem. Phys. **9**, 4414 (2007).
[21] S. Marinakis, G. Paterson, G. Richmond, M. Rockingham, M. L. Costen, and K. G. McKendrick, J. Chem. Phys. **128**, 021101 (2008).
[22] G. Paterson, S. Marinakis, M. L. Costen, K. G. McKendrick, and J. Kłos, J. Chem. Phys. **129**, 074304 (2008).
[23] G. Paterson, S. Marinakis, J. Kłos, M. L. Costen, and K. G. McKendrick, Phys. Chem. Chem. Phys. **11**, 8804 (2009).
[24] G. Paterson, S. Marinakis, M. L. Costen, and K. G. McKendrick, Phys. Chem. Chem. Phys. **11**, 8813 (2009).
[25] I. Ballingall, M. Rutherford, K. McKendrick, and M. Costen, Mol. Phys. **108**, 847 (2010).
[26] P. J. Dagdigian and M. H. Alexander, J. Chem. Phys. **130**, 094303 (2009).
[27] P. J. Dagdigian and M. H. Alexander, J. Chem. Phys. **130**, 164315 (2009).
[28] P. J. Dagdigian and M. H. Alexander, J. Chem. Phys. **130**, 204304 (2009).
[29] L. Ma, M. H. Alexander, and P. J. Dagdigian, J. Chem. Phys. **134**, 154307 (2011).

[30]G. Paterson, M. L. Costen, and K. G. McKendrick, Mol. Phys. **109**, 2565 (2011).
[31]G. Paterson, M. L. Costen, and K. G. McKendrick, Int. Rev. Phys. Chem. **31**, 69 (2012).
[32]R. T. Carter and J. R. Huber, Chem. Soc. Rev. **29**, 305 (2000).
[33]M. L. Costen, S. Marinakis, and K. G. McKendrick, Chem. Soc. Rev. **37**, 732 (2008).
[34]B. L. Hemming, D. R. Crosley, J. E. Harrington, and V. Sick, J. Chem. Phys. **115**, 3099 (2001).
[35]J. H. Lehman, M. I. Lester, J. Kłos, M. H. Alexander, P. J. Dagdigian, D. Herráez-Aguilar, F. J. Aoiz, M. Brouard, H. Chadwick, T. Perkins, and S. A. Seamons, J. Phys. Chem. A **117**, 13481 (2013).
[36]J. Kłos, M. H. Alexander, R. Hernández-Lamoneda, and T. G. Wright, J. Chem. Phys. **129**, 244303 (2008).
[37]M. H. Alexander and S. L. Davis, J. Chem. Phys. **78**, 6754 (1983).
[38]B. Follmeg, P. Rosmus, and H.-J. Werner, J. Chem. Phys. **93**, 4687 (1990).
[39]M. P. de Miranda and D. C. Clary, J. Chem. Phys. **106**, 4509 (1997).
[40]M. P. de Miranda, F. J. Aoiz, L. Bañares, and V. S. Rábanos, J. Chem. Phys. **111**, 5368 (1999).
[41]M. P. de Miranda and F. J. Aoiz, Phys. Rev. Lett. **93**, 083201 (2004).
[42]M. P. de Miranda, F. J. Aoiz, M. Brouard, and V. Sáez-Rábanos, J. Chem. Phys. **121**, 9830 (2004).
[43]F. J. Aoiz, J. E. Verdasco, V. J. Herrero, V. S. Rábanos, and M. H. Alexander, J. Chem. Phys. **119**, 5860 (2003).
[44]J. C. Tully and R. K. Preston, J. Chem. Phys. **55**, 562 (1971).
[45]J. C. Tully, J. Chem. Phys. **93**, 1061 (1990).
[46]E. Fabiano, T. W. Keal, and W. Thiel, Chem. Phys. **349**, 334 (2008).
[47]HIBRIDON is a package of programs for the time-independent quantum treatment of inelastic collisions and photodissociation written by M. H. Alexander, D. E. Manolopoulos, H.-J. Werner, B. Follmeg, P. J. Dagdigian, Q. Ma and others. For more information, see http://www2.chem.umd.edu/groups/alexander/hibridon.
[48]D. E. Manolopoulos, J. Chem. Phys. **85**, 6425 (1986).
[49]M. H. Alexander and D. E. Manolopoulos, J. Chem. Phys. **86**, 2044 (1987).
[50]K. H. Gericke, S. Klee, F. J. Comes, and R. N. Dixon, J. Chem. Phys. **85**, 4463 (1986).
[51]A. U. Grunewald, K. H. Gericke, and F. J. Comes, J. Chem. Phys. **89**, 345 (1988).
[52]R. N. Dixon, J. Nightingale, C. M. Weston, and X. Yang, Chem. Phys. Lett. **151**, 328 (1988).
[53]K. H. Gericke, H. G. Gläser, C. Maul, and R. N. Dixon, J. Chem. Phys. **92**, 411 (1990).
[54]M. P. Docker, A. Hodgson, and J. P. Simons, Faraday Discuss. Chem. Soc. **82**, 25 (1986).
[55]J. August, M. Brouard, M. P. Docker, A. Hodgson, C. J. Milne, and J. P. Simons, Ber. Bunsen-Ges. Phys. Chem. **92**, 264 (1988).
[56]M. Brouard, M. T. Martinez, C. J. Milne, and J. P. Simons, Chem. Phys. Lett. **165**, 423 (1990).
[57]A. J. Alexander, Phys. Rev. A **66**, 060702 (2002).
[58]A. J. Alexander, J. Chem. Phys. **118**, 6234 (2003).
[59]Y.-P. Chang, M. Brouard, R. Cireasa, T. Perkins, and S. A. Seamons, Phys. Chem. Chem. Phys. **13**, 8213 (2011).
[60]J. Luque and D. R. Crosley, LIFBASE: Database and Simulation Program (v. 1.6), SRI International Report MP 99-009, 1999.
[61]P. Lebow, F. Raab, and H. Metcalf, Phys. Rev. Lett. **42**, 85 (1979).
[62]F. Raab, T. Bergman, D. Lieberman, and H. Metcalf, Opt. Lett. **5**, 427 (1980).
[63]F. Raab, T. Bergman, D. Lieberman, and H. Metcalf, Phys. Rev. A **24**, 3120 (1981).
[64]R. T. Carter, I. M. Povey, H. Bitto, and J. R. Huber, J. Chem. Phys. **104**, 5365 (1996).
[65]J. Xin and S. A. Reid, J. Chem. Phys. **112**, 10067 (2000).
[66]J. Xin and S. A. Reid, J. Chem. Phys. **116**, 525 (2002).
[67]J. Xin, I. Ionescu, D. Kuel, and S. A. Reid, Chem. Phys. **291**, 61 (2003).
[68]K. R. German and R. N. Zare, J. Chem. Phys. **54**, 4039 (1971).
[69]P. J. Brucat and R. N. Zare, J. Chem. Phys. **78**, 100 (1983).
[70]P. J. Brucat and R. N. Zare, J. Chem. Phys. **81**, 2562 (1984).
[71]M. Brouard, I. Burak, S. D. Gatenby, D. Hart, and D. Minayev, J. Chem. Phys. **110**, 11335 (1999).
[72]P. H. Paul, J. Phys. Chem. **99**, 8472 (1995).
[73]B. L. Hemming, D. R. Crosley, J. E. Harrington, and V. Sick, J. Phys. Chem. A **106**, 8992 (2002).